GENERATION OF SYNTHETIC FLAIR MRI IMAGE FROM REAL CT IMAGE FOR ACCURATE SYNOVIAL FLUID SEGMENTATION IN HUMAN KNEE IMAGE

I.F. Abu-Qasmieh[*], I.S. Masad[*], H. Alquran[*], K.Z. Alawneh[†]

Abstract: Synthetic MRI FLAIR images of an abdominal 3D multimodality phantom and *in vivo* human knee have been generated from real CT images using predefined mapping functions of CT mean and standard deviation with the corresponding proton density PD, T_1 and T_2 that were previously generated from spin-echo sequence. First, the validity of generating synthetic MR images from different sequences were tested and the same PD, T_1 and T_2 maps that were generated from the real CT image have been used in the simulation of MRI inversion-recovery (IR) sequence. The similarity results between the real and synthetic IR sequence images, using different inversion times T_I, showed a very good agreement. After confirming the feasibility of generating synthetic IR images from the PD, T_1 and T_2-maps, that were originally obtained from spin-echo sequence using the phantom, the simulation of a knee image has been generated from the corresponding knee CT real image using the steady-state transverse magnetization formula of the inversion-recovery sequence. The simulated FLAIR IR sequence MR image are generated using proper T_I for nulling the signal from the synovial fluid, where the image complement is used as a mask for segmenting the corresponding tissue region in the real CT image.

Key words: *synthetic MRI, computed tomography, spin-echo, inversion recovery, FLAIR, knee synovial fluid*

Received: December 4, 2022 **DOI:** 10.14311/NNW.2023.33.012
Revised and accepted: June 30, 2023

1. Introduction

Fluid-attenuated inversion recovery (FLAIR) is an MRI sequence with an inversion recovery setup to nullify fluids signal in the output image where the inversion time T_I is selected such that there is no net longitudinal magnetization M_z at equilibrium

[*]Isam F. Abu-Qasmieh; Ihssan S. Masad – Corresponding author; Hiam Alquran; Department of Biomedical Systems and Informatics Engineering, Yarmouk University, Jordan, E-mail: iabuqasmieh@yu.edu.jo

[†]Khaled Z. Alawneh; Faculty of Medicine, Jordan University of Science and Technology, King Abdullah University Hospital, Jordan.

from the fluid voxels, and therefore, their contribution to the resultant image is nulled [1].

Several studies have addressed the generation of synthetic MR images based on other modality or based on MR quantification, where such techniques reduce examination time while providing quantitative measurements of clinical and research interests [2–8]. Such studies reported that synthetic images with different proton density PD, T_1 and T_2 weightings are acceptable diagnostic tools with similar effectiveness as the conventional imaging.

For synthetic FLAIR images, several artifacts were reported as a bright signal appeared due to flow and partial volume effects, which are considered in the analytical signal of real-synthetic mapping models. Other models that generated synthetic FLAIR images based on deep learning using convolutional neural network have shown promising results for similar problems in which mapping model-based analytical techniques are difficult to implement [9, 10]. Abu-Qasmieh et al. [11] showed in their study the effectiveness of generating synthetic MR images with different weightings from a real CT image by building CT mean and standard deviation mapping functions with the corresponding intrinsic parameters namely, PD, T_1 and T_2 in the MR mages of the same slice in 3D multimodality abdominal phantom and on human knees at different T_{E} and T_{R} parameters using a spin-echo sequence.

In this study, the generation of synthetic MR images in [11] is extended by using the same CT-MRI mapping functions to generate the PD, T_1 and T_2 maps for the simulation of another MRI sequence, particularly the inversion recovery FLAIR sequence by using the proper inversion time T_{I} for nulling the synovial fluid signal from the knee FLAIR simulated image and then segmenting the corresponding tissue from the real CT image.

2. Materials and method

2.1 CT imaging

The dataset of [11] is used in this study, where the CT images were acquired, with proper acquisition parameters for a selected slice of a triple-modality 3D abdominal phantom. The CT image acquisition was repeated 9 times for averaging to increase the signal-to-noise ratio (SNR).

2.2 MR imaging

The same slice acquired using the CT scanner was imaged with a clinical 1.5-T MRI system. MR images, used to generate the three contrast MRI maps, were acquired using a spin echo (SE) pulse sequence using similar slice imaging dimension, size and thickness used in CT imaging.

For T_1-map and ρ-map calculations, a series of MR images was acquired for the same slice with echo time $T_{\mathrm{E}} = 20\,\mathrm{ms}$ and repetition times $T_{\mathrm{R}} = 100, 200, 400, 800, 1250, 2000, 4000,$ and $5000\,\mathrm{ms}$. For T_2-map calculation, another series of MR images was acquired with $T_{\mathrm{E}} = 10, 15, 25, 40, 60, 90, 130, 180, 240\,\mathrm{ms}$ and $T_{\mathrm{R}} = 2000\,\mathrm{ms}$ [11].

The amplitude of the spin-echo signal is given by:

$$A_{\mathrm{E}} = \rho \left(1 - 2e^{-\frac{(T_{\mathrm{R}} - T_{\mathrm{E}}/2)}{T_1}} + e^{-\frac{T_{\mathrm{R}}}{T_1}}\right) e^{-\frac{T_{\mathrm{E}}}{T_2}} \tag{1}$$

If $T_{\mathrm{E}} \ll T_{\mathrm{R}}$, Eq. (1) can be simplified to:

$$A_{\mathrm{E}} = \rho \left(1 - e^{-T_{\mathrm{R}}/T_1}\right) e^{-T_{\mathrm{E}}/T_2} \tag{2}$$

The acquired CT and MR series images with T_1, T_2, and ρ weightings were subjected to two main processes: registration and segmentation. The corresponding flow chart in Fig. 1 summarizes the methodology followed by this study.

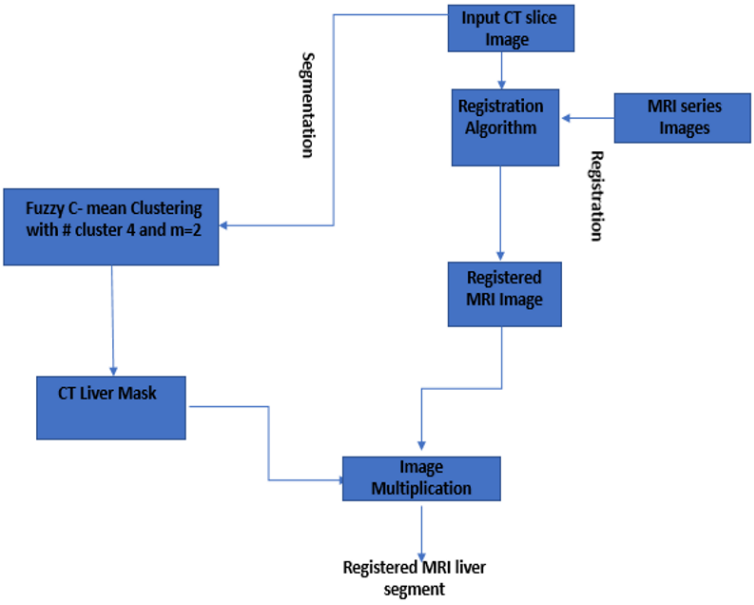

Fig. 1 *The registration and segmentation processes.*

2.3 Maps calculations

The calculations of T_1, T_2, and ρ-maps were described in [11]; however, they are repeated in this work for better readability and flow of information.

T_1-map calculation Eq. (1) can be re-written as a function of T_{R}:

$$A_{\mathrm{E}}(b) = C_1 + C_2 b^{C_3}, \tag{3}$$

where

$$\begin{aligned} b &= e^{-T_{\mathrm{R}}}, \\ C_1 &= \rho e^{-T_{\mathrm{E}}/T_2}, \\ C_2 &= -\rho e^{-T_{\mathrm{E}}/T_2}\left(2e^{-T_{\mathrm{E}}/2T_1} - 1\right), \end{aligned}$$

and

$$C_3 = 1/T_1 \quad \text{or} \quad T_1 = 1/C_3. \tag{4}$$

T_2-map calculation Eq. (2) can be manipulated to:

$$\ln(A_{\mathrm{E}}) = C_1 + C_2 T_{\mathrm{E}}, \tag{5}$$

where

$$C_1 = \ln\left(\rho\left(1 - e^{-T_{\mathrm{R}}/T_1}\right)\right),$$

and

$$C_2 = -1/T_2 \quad \text{or} \quad T_2 = -1/C_2. \tag{6}$$

ρ-map calculation Proton density map is derived from the image series with different T_{R} using the following equation:

$$A_{\mathrm{E}}(x) = \rho x, \tag{7}$$

where

$$x = \left(1 - 2e^{-\frac{(T_{\mathrm{R}} - T_{\mathrm{E}}/2)}{T_1}} + e^{-\frac{T_{\mathrm{R}}}{T_1}}\right) e^{-\frac{T_{\mathrm{E}}}{T_2}}. \tag{8}$$

2.4 MRI maps

Fig. 2 shows the reference CT image for the selected slice, from which the liver region was segmented and five ROI's were selected, as shown in Fig. 3, to illustrate the approach analysis.

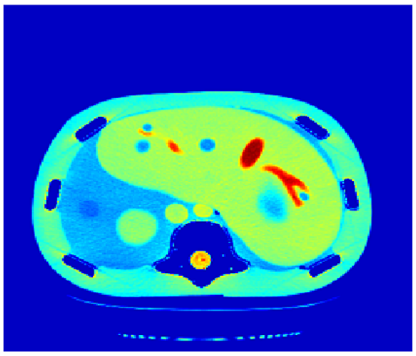

Fig. 2 *The selected CT slice reference image [11].*

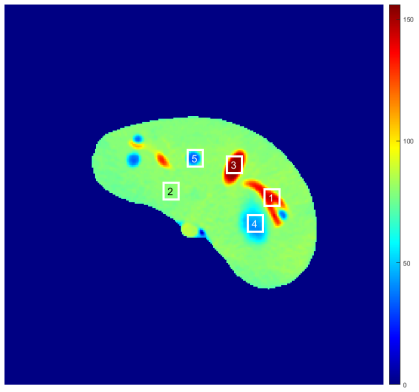

Fig. 3 *The liver partition segmentation [11].*

T_1-map Eq. (3) was used to calculate the T_1 value for each pixel in the liver segment, where b was plotted versus A_{E} (Fig. 4) and the equation of the best fitting line was found to calculate C_3, and consequently, T_1 value.

T_2-map On the other hand, Eq. (5) was used to calculate the T_2 value for each pixel in liver segment, where T_{E} was plotted versus the natural logarithm of the

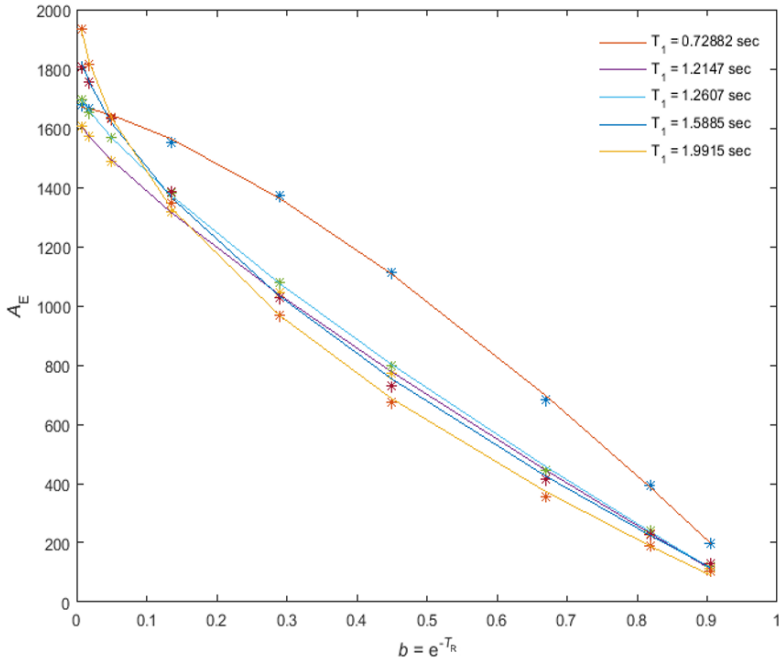

Fig. 4 *Fitting curves of the signal A_{E} with $e^{-T_{\mathrm{R}}}$ at different locations (indicated in Fig. 3) of the selected slice with their corresponding calculated T_1 relaxation times.*

gray-level ($\ln A_{\mathrm{E}}$) for different positions as shown in Fig. 5; and the equation of the best fitting line was found to calculate C_2 in order to obtain the T_2 value.

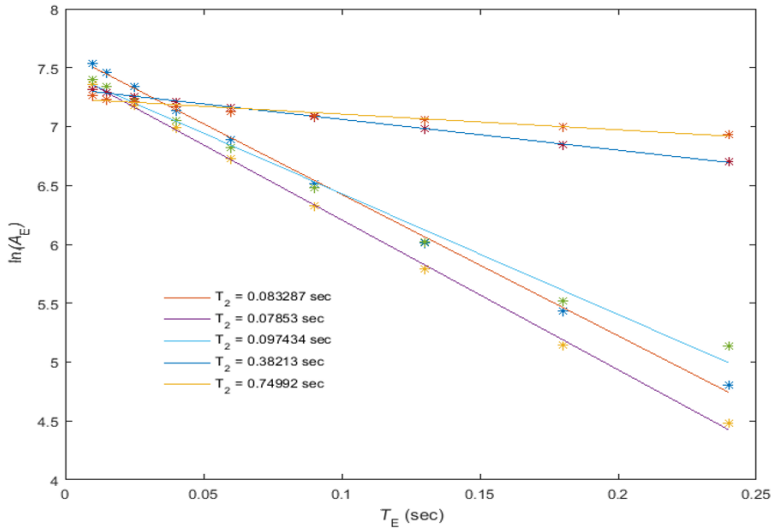

Fig. 5 *Fitting curves of the signal $ln(A_{\mathrm{E}})$ with T_{E} at different locations (indicated in Fig. 3) of the selected slice with their corresponding calculated T_2 relaxation times.*

ρ-maps Finally, the same images used to calculate the T_1 map were used to calculate the proton density map (ρ-map). The linear fittings for the different positions in liver ROI with their calculated ρ are displayed in Fig. 6.

The three maps of the main contrast parameters for the selected phantom slice are shown in Fig. 7 for comparison.

2.5 Mapping between CT and MRI contrast parameters

For mapping the CT of the liver segment in the reference CT image to the MRI contrast parameters of the same segment, the liver partition was reshaped to a vector (one-dimensional array) in the four images for fitting purposes. The mapping was performed between the mean and the standard deviation values extracted from the CT of each liver pixel and its surrounding neighbors of a window size 5×5. The resultant surface fitting using piecewise linear interpolation between each contrast parameter and the corresponding CT mean μ and standard deviation σ values are illustrated in Fig. 8, where the three mapping functions were obtained and saved for achieving the goal of generating synthetic MR images from a real CT image.

2.6 Inversion recovery MRI sequence

The phantom's slice for the real CT image selected in the study of [11] was used for testing the proposed approach. The same slice was imaged by clinical 1.5-T MRI

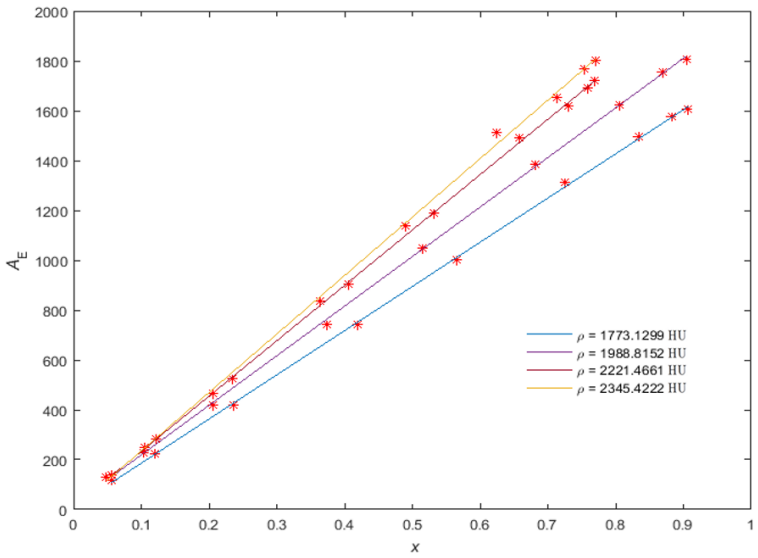

Fig. 6 *Fitting curves of the signal A_E with x at different locations (indicated in Fig. 3) of the selected slice with their corresponding calculated proton density ρ.*

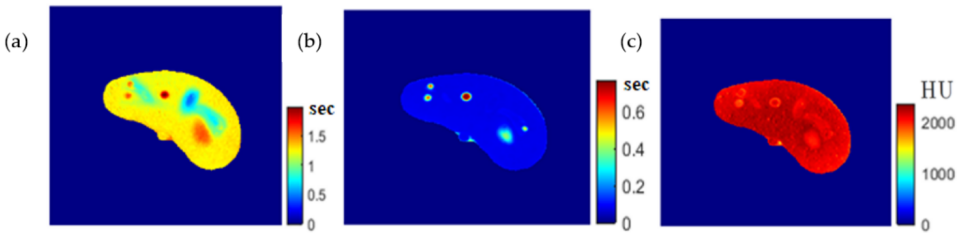

Fig. 7 *The calculated T_1-map (a), T_2-map (b), and ρ-map (c) of the liver segment in the selected phantom slice [11].*

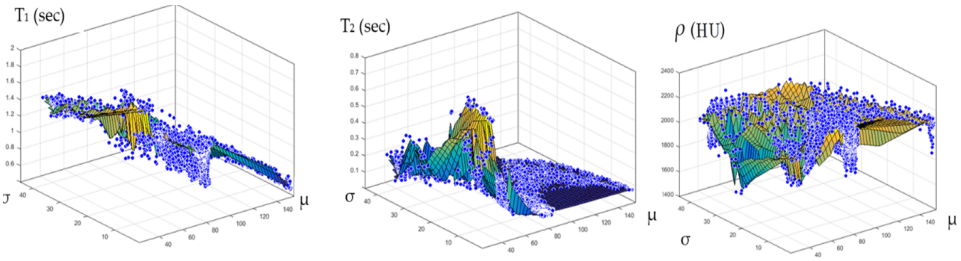

Fig. 8 *The surface fitting for CT-MRI mapping, using piecewise linear interpolation between the contrast parameters (T_1, T_2, and ρ), and the corresponding CT mean μ and standard deviation σ values (left, middle, and right graphs, respectively) [11].*

system (Optima MR360, GE Healthcare, Chicago, IL, USA) using the inversion-recovery sequence protocol with the following parameters: slice thickness = 2.5 mm, FOV = 30 cm × 30 cm, matrix size = 256 × 256 pixels, bandwidth = 15.6 kHz, echo time T_{E}) = 10 ms and repetition times T_{R} = 2540 ms and inversion times $T_{\mathrm{I}} = 100, 250, 500, 750, 1000, 1250, 1500, 1750, 2000$ and 2500 ms. The MR IR image was acquired to compare MR real image with the simulated ones and to test the validity using the CT-MR spin-echo PD (ρ), T_1 and T_2 functions in generating synthetic images using different MR sequences.

For simulation purposes, the IR pulse sequence steady state signal equation is used as follows [12]:

$$A_{\mathrm{E}} = \rho \left(1 - 2e^{-\frac{T_{\mathrm{I}}}{T_1}} + 2e^{-\frac{(T_{\mathrm{R}} - T_{\mathrm{E}}/2)}{T_1}} - e^{-\frac{T_{\mathrm{R}}}{T_1}}\right) e^{-\frac{T_{\mathrm{E}}}{T_2}}, \tag{9}$$

when $T_{\mathrm{E}} \ll T_1$, Eq. (9) can be simplified to:

$$A_{\mathrm{E}} = \rho \left(1 - 2e^{-\frac{T_{\mathrm{I}}}{T_1}} + e^{-\frac{T_{\mathrm{R}}}{T_1}}\right) e^{-\frac{T_{\mathrm{E}}}{T_2}}, \tag{10}$$

where according to Eq. (10), the tissue signal can be nulled if the inversion time T_{I} is chosen as:

$$T_{\mathrm{I}} = T_1 \ln\left(\frac{2}{1 + e^{-\frac{-T_{\mathrm{R}}}{T_1}}}\right). \tag{11}$$

3. Results and discussion

The acquired real IR MR images were compared with the simulated/synthetic corresponding images, after image registration, using the same technical parameters, $T_{\mathrm{E}}, T_{\mathrm{R}}$ and T_{I} and Eq. (10) to investigate the validity of the proposed approach. The similarities between the generated synthetic MR images from the real CT image and the real MR images of the same slice were tested using two parameters; the slope between the generated/synthetic MR image segment array (liver segment) and the real MR image segment array after they have been reshaped to vectors. The other similarity testing parameter used is the percentage root-mean-square difference (PRD).

Fig. 9 shows the real and the generated MR images with T_{E} = 10 ms, T_{R} = 2540 ms and inversion times, $T_{\mathrm{I}} = 100, 250, 500, 750, 1000, 1250, 1500, 1750, 2000$ and 2500 ms, respectively, with the similarity relationship of their liver segments after they were reshaped to vectors, where the calculated similarity parameters of slope/PRD were (0.999/5.36%, 0.991/2.54%, 0.961/12.71%, 1.008/5.06%, 0.997/2.83%, 0.987/2.25%, 0.991/1.82%, 0.983/1.65%, 0.985/1.64%, 1.004/1.42%), respectively.

After the very good agreement of the MR synthetic image with the corresponding MR real image, the same approach was implemented for the human knee slice [11] using the saved mapping functions of the CT real image with the three contrast intrinsic maps T_1, T_2 and PD (ρ)-maps. Fig. 10 shows the real CT knee image, while the corresponding generated MRI maps are shown in Fig. 11.

The simulated/synthesized IR FLAIR MR image of the corresponding CT image shown in Fig. 10 was generated using Eq. (10) and parameters T_{E} = 10 ms, T_{R} =

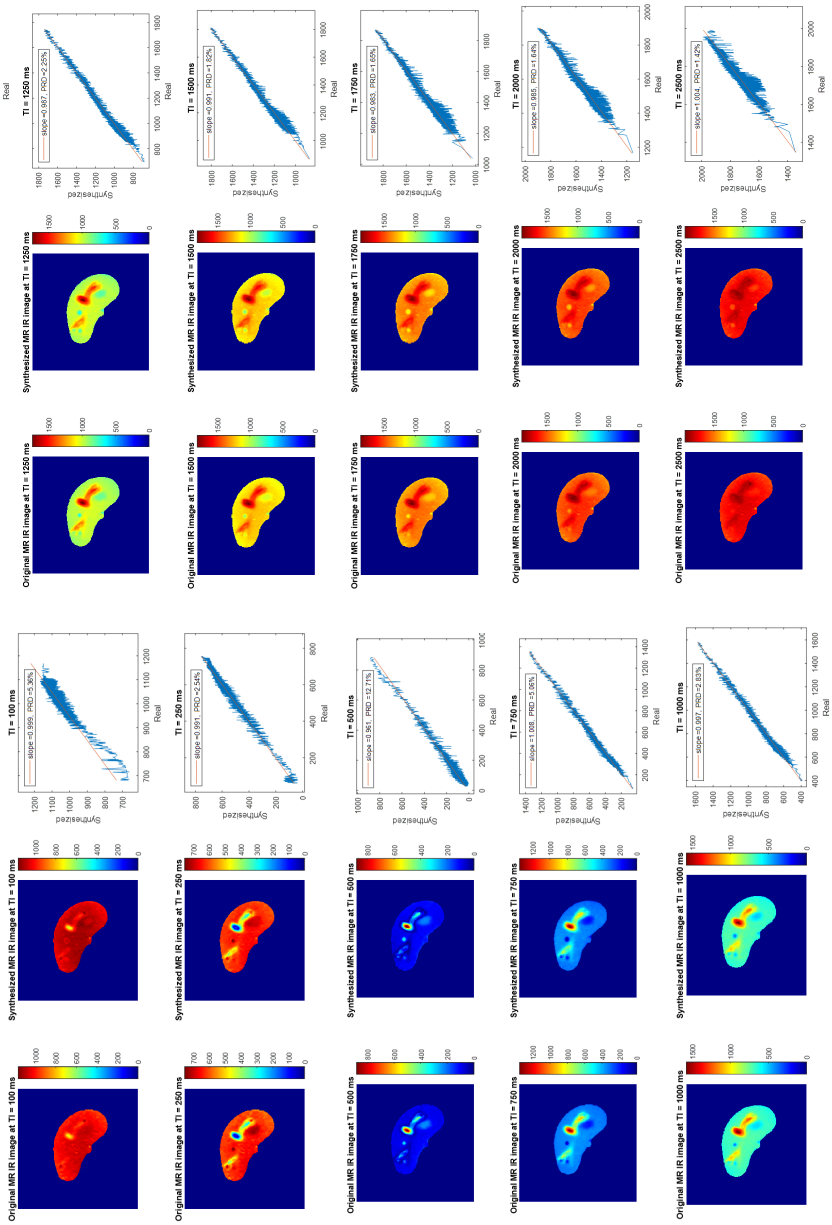

Fig. 9 *The real/original inversion recovery images at the left, the corresponding synthesized/simulated images at the middle and the similarity results between the real and synthesized images at the right for different* T_I.

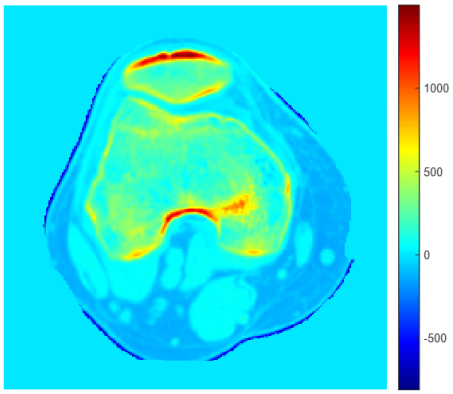

Fig. 10 *The real CT image of a selected human knee slice in HU [11].*

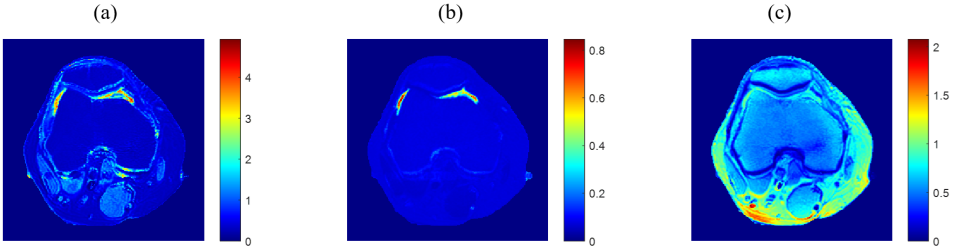

Fig. 11 *(a) The generated T_1-map in sec, (b) T_2-map in sec, and (c) ρ-map in HU, generated from the real CT image shown in Fig. 14 [11].*

2540 ms and T_I is calculated such that the synovial fluid signal is nulled in the knee IR image using Eq. (11). The T_1 relaxation time for the synovial fluid in the human knee at field strength 1.5 T is around 2641 ± 60 ms [13] and therefore, the T_I for nulling the synovial fluid signal is around 976 ms. The generated FLAIR image using the proper T_I is shown in Fig. 12 with its complement image.

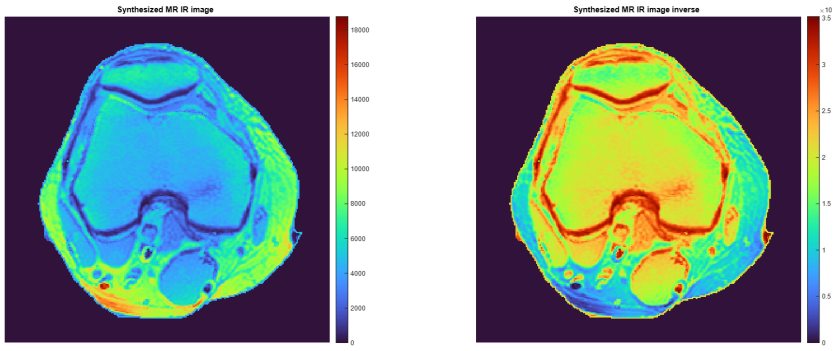

Fig. 12 *The synthesized knee FLAIR image (left) with its inverse (right).*

The complement image shown in Fig. 12 was gray-level transformed by power of three (cubed) to enhance the high gray level of the synovial fluid region and the result was then binarized as shown in Fig. 13. After suppression the signal of the synovial fluid using proper T_{I} value, which permits a clear and accurate determination of the concerned tissue, the image complement, to inverse the low signal pixels to have the maximum intensity, was calculated and then binarized by thresholding to obtain the synovial fluid mask as shown in Fig. 13.

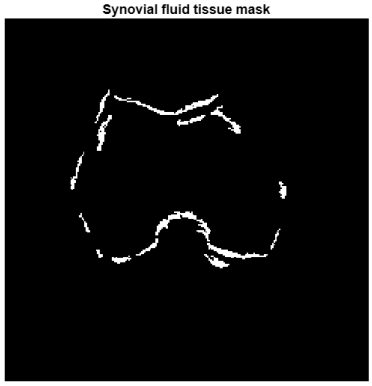

Fig. 13 *The synovial fluid region mask is generated using proper binarization threshold.*

The synovial fluid region mask was then multiplied by the original/real CT image shown in Fig. 10. for segmentation of the synovial fluid region from the CT image as shown in Fig. 14.

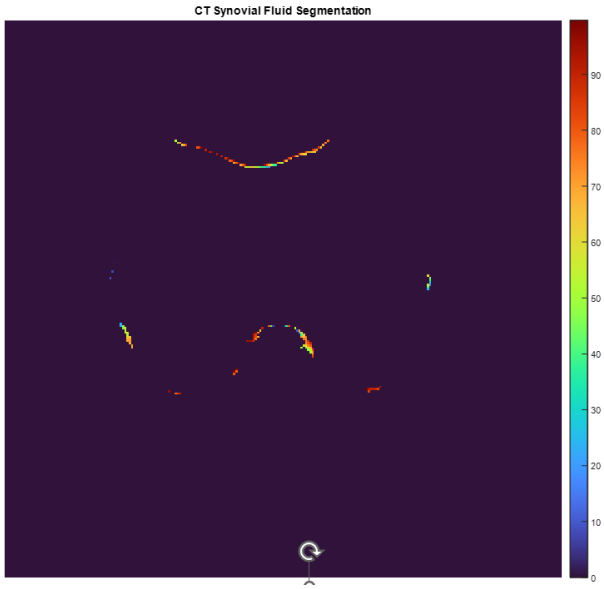

Fig. 14 *The segmented synovial fluid region, in HU, from the original CT image.*

The segmented synovial fluid region using the proposed simulation method was delineated clearly compared to the conventional CT windowing method, using piecewise gray level transformation for well-defined tissue type (synovial fluid) window width and window center (Fig. 15) used for displaying specific tissue in CT image after windowing the synovial fluid region.

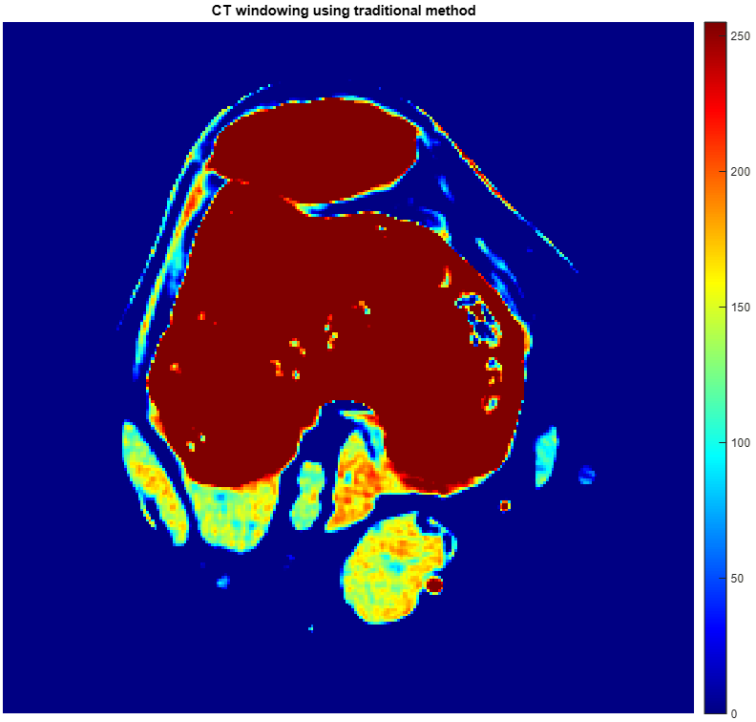

Fig. 15 *The synovial fluid CT windowing result using the traditional method.*

4. Conclusion

This study has been designed to compare the overall image quality of synthetic/simulated MR imaging with conventional/real MR imaging in inversion recovery sequence. Other objectives included legibility of anatomic features and diagnostic performance of synovial fluid region in human knee axial image using FLAIR pulse sequence. The current study has validated the assumption that once the MRI three main intrinsic contrast parameters maps, T_1, T_2 and PD (ρ), have been generated using predefined mapping functions with the corresponding CT image, other MRI pulse sequences images can be generated with similar diagnostic quality using the steady state formula of that specific MR pulse sequence. In addition, synthetic MRI generation was significantly faster than conventional MRI scanning if many different contrast settings were required for the same geometry, which is usually applicable for clinical examinations. Moreover, the FLAIR synthetic image permits

the accurate delineation of the fluid region from the corresponding CT real image, which supports taking the correct diagnostic decision by the specialist radiologist.

References

[1] ESSIG M., BOCK M. Contrast optimization of fluid-attenuated inversion-recovery (FLAIR) MR imaging in patients with high CSF blood or protein content. *Magnetic Resonance in Medicine*. 2000, 43(5), pp. 764–767, doi: 10.1002/(sici)1522-2594(200005)43:5<764::aid-mrm21>3.0.co;2-f.

[2] WEST J. *Quantitative Magnetic Resonance Imaging of the Brain: Applications for Tissue Segmentation and Multiple Sclerosis*; 2014. PhD thesis, Linköping University Electronic Press.

[3] GRANBERG T., UPPMAN M., HASHIM F., CANANAU C., NORDIN L.E., SHAMS S., BERGLUND J., FORSLIN Y., ASPELIN P., FREDRIKSON S., KRISTOFFERSEN-WIBERG M., Clinical feasibility of synthetic MRI in multiple sclerosis: a diagnostic and volumetric validation study. *American Journal of Neuroradiology*. 2016, 37(6), pp. 1023–1029, doi: 10.3174/ajnr.a4665.

[4] BETTS A.M., LEACH J.L., JONES B.V., ZHANG B., SERAI S. Brain imaging with synthetic MR in children: clinical quality assessment. *Neuroradiology*. 2016, 58(10), pp. 1017–1026, doi: 10.1007/s00234-016-1723-9.

[5] HAGIWARA A., WARNTJES M., HORI M., ANDICA C., NAKAZAWA M., KUMAMARU K.K., ABE O., AOKI S., SyMRI of the Brain. *Investigative Radiology*. 2017, 52(10), pp. 647–657, doi: 10.1097/rli.0000000000000365.

[6] HAGIWARA A., HORI M., YOKOYAMA K., TAKEMURA M.Y., ANDICA C., TABATA T., KAMAGATA K., SUZUKI M., KUMAMARU K.K., NAKAZAWA M., TAKANO N. Synthetic MRI in the Detection of Multiple Sclerosis Plaques. *American Journal of Neuroradiology*. 2016, 38(2), pp. 257–263, doi: 10.3174/ajnr.a5012.

[7] TANENBAUM L.N., TSIOURIS A.J., JOHNSON A.N., NAIDICH T.P., DELANO M.C., MELHEM E.R., QUARTERMAN P., PARAMESWARAN S.X., SHANKARANARAYANAN A., GOYEN M., FIELD A.S. Synthetic MRI for Clinical Neuroimaging: Results of the Magnetic Resonance Image Compilation (MAGiC) Prospective, Multicenter, Multireader Trial. *American Journal of Neuroradiology*. 2017, 38(6), pp. 1103–1110, doi: 10.3174/ajnr.a5227.

[8] HAN C., HAYASHI H., RUNDO L., ARAKI R., SHIMODA W., MURAMATSU S., FURUKAWA Y., MAURI G., NAKAYAMA H. GAN-based synthetic brain MR image generation. In: *2018 IEEE 15th international symposium on biomedical imaging (ISBI 2018)*. 2018, pp. 734–738.

[9] RYU K., NAM Y., GHO S.M., JANG J., LEE H.J., CHA J., BAEK H.J., PARK J., KIM D.H. Data-driven synthetic MRI FLAIR artifact correction via deep neural network. *Journal of Magnetic Resonance Imaging*. 2019, 50(5), pp. 1413–1423, doi: 10.1002/jmri.26712.

[10] LEE D., LEE J., KO J., YOON J., RYU K., NAM Y. Deep learning in MR image processing. *Investigative Magnetic Resonance Imaging*. 2019, 23(2), pp. 81–99, doi: 10.13104/imri.2019.23.2.81.

[11] ABU-QASMIEH I.F., MASAD I.S., AL-QURAN H.H., ALAWNEH K.Z. Generation of Synthetic-Pseudo MR Images from Real CT Images. *Tomography*. 2022, 8(3), pp. 1244–1259, doi: 10.3390/tomography8030103.

[12] KUPERMAN V. *Magnetic resonance imaging: physical principles and applications*. Elsevier, 2000.

[13] VAN LEEUWEN F.H., LENA B., ZWANENBURG J.J., VAN VULPEN L.F., BARTELS L.W., FISCHER K., NAP F.J., DE JONG P.A., BOS C., FOPPEN W. Detecting low blood concentrations in joints using T1 and T2 mapping at 1.5, 3, and 7 T: an in vitro study. *European Radiology Experimental*. 2021, 5(1), pp. 1–10, doi: 10.1186/s41747-021-00251-z.